ORIGINAL ARTICLE

Effect of process parameters on pulsed laser welding of AA5083 alloy using response surface methodology and pulse shape variation

Mariane Chludzinski[1] · Rafael Eugenio dos Santos[1] · Cristina Churiaque[1] · Marta Ortega-Iguña[1] · Jose Maria Sánchez-Amaya[1]

Abstract

Aluminium alloys exhibit eco-friendly aspects related to global environmental issues, such as almost unlimited recyclability. Nevertheless, some intrinsic characteristics are challenges to explore all their benefits. In the welding process, the high thermal conductivity and low melt point require high control of heat input. Alternatively, the pulsed laser mode provides a sharp beam focus with precise control enabling regulating the energy delivered. In this sense, this present work analysed the effect of pulsed laser welding parameters on 3-mm-thick AA5083 aluminium alloy sheets. Trials targeted to develop sound welds with minimum defect and high penetration depth adopting statistical methods. The optimum parameter arrangement was achieved by varying peak power, spot diameter, and pulse duration. Finally, the best parameter combination was applied using different pulse shapes to mitigate crack formation and pores. As a result, the pulse shape with step-down at the end of each pulse generated crack-free spot welds.

Keywords AA5083 · Pulsed laser welding · Pulse shape · Response surface methodology · Microstructure

1 Introduction

From the current global demand for reducing environmental impact, industries have constantly investigated sustainable processes and products. In terms of materials, aluminium has inherent characteristics as an almost endlessly recyclable for supporting green requirements. In addition, some aluminium alloys provide advantages over other materials with high strength or high-cycle fatigue resistance combined with corrosion resistance and low cost [1]. For this reason, several industries from electronics, aerospace, aeronautical, automotive, and naval field have been widely adding aluminium components in their products, as structural components, skin shapes, cables, and building supplies [1–3].

However, intrinsic aluminium properties, such as high thermal conductivity and reflectivity besides low viscosity and melting point, display challenges regarding the welding procedures. In pure aluminium, the thermal conductivity achieves 200 W/m K [4]. Therefore, the heat input delivered on the material rapidly spreads the energy from the weld pool. Even adding the alloying elements to reduce the thermal conductivity (reaching about 110 W/m K), the high heat conduction, and low melting point require special procedures of the arc welding [5]. The high heat input can affect all components during the welding, and temperature control is necessary. Besides, the extended period in the liquid phase increases the diffusion of hydrogen into the welding pool. To avoid this, joining aluminium alloys requires the use of high heat input density. This characteristic is present in laser technology, where the laser beam delivers high energy in a small sharp area. As well as the concentrated heat source, this process is flexible and efficiently joins components that

✉ Mariane Chludzinski
  mariane.chludzinski@uca.es

  Rafael Eugenio dos Santos
  rafaeleugeniodossantos@gmail.com

  Cristina Churiaque
  cristina.churiaque@uca.es

  Marta Ortega-Iguña
  marta.ortega@uca.es

  Jose Maria Sánchez-Amaya
  josemaria.sanchez@uca.es

1   Department of Materials Science and Metallurgical
    Engineering and Inorganic Chemistry, LABCYP, Faculty
    of Engineering, University of Cádiz, Av. Universidad de
    Cádiz 10, 11519 Puerto Real (Cádiz), Spain

require dimensional accuracy [1, 6–10]. Nevertheless, the high reflectivity can compromise the laser beam efficiency causing a reduction in the absorption of the incident radiation [5].

Laser welding methodology is commonly distinguished as continuous, pulsed, and recent intermediary mode. In continuous mode, high laser power sources enable producing weld seams with fast welding scan. However, the low welding velocity from the pulsed laser mode allows joining with control and accuracy of welding parameters. It promotes concentrated heat affect zones with minimal mechanical stress and low distortion [2, 11–16]

Several investigations of pulsed laser process applied on aluminium alloys have been accomplishing sound welds through proper parameter combinations [5]. However, some alloys have presented specific adversities that can generate defects such as shallow penetration, porosities, blowholes, and solidification cracks. Some studies have demonstrated that the cracking phenomenon is affected by the thermal history, chemical composition, and eutectic fractions [1, 2, 17, 18]. As describe by Hekmatjou and Naffakh-Moosavy [2], the fast cooling rates increased the crack sensitivity. The quick solidification abbreviated the time for the liquid to fill the intergranular spaces. Other researches indicate that during the solidification process, the temperature near the solidus facilitated the development of very thin liquid films within the grain boundaries. In the subsequent cooling stage, these films can be insufficient to fill the spaces between the solidified materials. These lacks of intergranular cohesion create a tendency to display crack due to the residual tensile stresses from the weld shrinkage [19, 20]. Furthermore, higher welding speed increased the cooling rate generating a specific condition to induce the crack formation due to the finer dendrite and grain size microstructure formations [2].

The variation of alloy element concentrations and impurities, especially those with low melting temperatures, affects the crack susceptibility [18]. Some alloying elements, such as Mg and Si, have been associated with the extended solidification temperature range [1]. Therefore, the adjustment of alloy composition enabled modifying the volume fractions and distribution of secondary phases with low melting points [21]. According to the hot crack susceptibility curve of Al–Mg alloys, the highest predisposition point is reached when the material displays around 2% Mg [17, 20, 22]. Investigations indicated that the energy achieved by the laser welding process reduced the Mg content into the welding pool. This effect is a consequence of the physical properties of Mg over an environment of high temperature

imposed by the laser beam. Therefore, in alloys with higher Mg content, the peak point susceptibility can be reached by the Mg evaporation [17, 20].

In this matter, investigations have analysed the crack susceptibility in the pulsed laser welding parameters applied on Al–Mg alloys. These well-known 5000 series alloys are non-heat-treatable and contain magnesium as the principal alloying element. This series has gained particular attention for structural applications due to the combination of high corrosion resistance and strength [2]. The study performed by Beiranvand et al. [17] with AA5083-H321 demonstrated that the cracking decreased when the pulse overlapping increased from 55 to 88%, which reduced the Mg content from 4.45 to 3.30 wt%. Abioye et al. [1] welded AA5052-H32 alloy using aluminium ER5356 wire. This work showed that a high dilution of alloying elements, e.g. Mg, formed cracks. In AA5052, parameters with 8.64 J pulse energy produced crack-free pulsed laser joint. The solidification rate limited the microsegregations generating a microstructure with fine precipitates homogeneously distributed [20].

Another approach usually employed to avoid the cracking formation, besides the process parameters selection, is the preheat treatment processes. Hekmatjou and Naffakh-Moosavy [2] observed that the crack tendency decreased with the pulse frequency increase from 40 to 60 Hz in AA5456 sheets. Nevertheless, only applying preheating between 150 and 300 °C resulted in free-crack welds. In this condition, the temperature ranges reduced the cooling and solidification rates. It resulted in a microstructure composed of equiaxed grains. Under this condition, the remained liquid and welding stresses were distributed uniformly, avoiding the crack sensitivity.

Besides the abovementioned methods, pulse laser technology provides the pulse shape configuration as another strategy to mitigate defects. Usually, pulsed laser beam profiles display a rectangular shape where the peak power is reached quickly, maintaining this level during the pulse. As an advantage of the laser process, the high accuracy and power control enable applying different peak power levels along the pulse time. Therefore, it allows adding stages before and after reaching the peak power. In the previous stage before the peak plateau, shapes can display linear ramp-up, leading-spike, or step-up. The post-peak power can be configured as linear ramp-down, step-down, and step-up shapes.

The exploration of these pulse shapes has considered that the peak power variation regulates the molten pool behaviour

Table 1 Chemical composition of AA5083

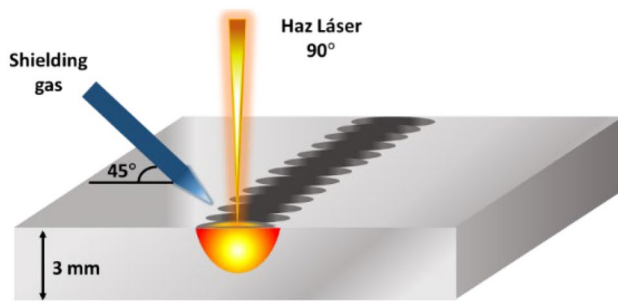| Element	Mn	Si	Cr	Cu	Zn	Fe	Ti	Mg	Al
wt %	0.471	0.155	0.135	0.068	0.074	0.295	0.022	4.850	Bal

Fig. 1 Welding setup

through the pre and post heating, changing the heating, and cooling rates as a consequence [23–27]. The work developed by Zhang and Cao [24] with 3-mm-thick AZ31 magnesium alloy showed that the prolonged slow cooling (from 2 to 10 ms) condensed the solidification cracking sensitivity, and the low step-down peak power suppressed the Mg evaporation bubbles in the keyhole welding condition. Rohde et al. [23] observed similar effects in bead-on-plate configuration of AlMg3 and AlMg4,5Mn sheets. In their work, the addition of the post-peak power step adjusted the cooling time and consequently controlled the pore formation and crack susceptibility. In AA5083 aluminium alloy, both ramp-down and step-down profiles produced crack-free joints due to solidification rate reduction [25]. Mizutani and Katayama [26] obtained similar outcomes with 5-mm-thick sheets of annealed AA5083 aluminium alloy with a step-down shape of 20 ms. In the 6000 series, Zhang et al. [27] demonstrated a limited range of trailing ramp-down gradients for producing AA6061-T6 crack-free weldments. However, varying the peak power (time and power) changed these limits.

In the present work, the influence of pulse laser welding parameters on AA5083-H111 aluminium alloy with 3-mm thickness was investigated. Differently from the abovementioned works, a design of experiment method was applied for the first time in this alloy to determine an optimal parameter combination, followed by a pulse shape analysis based on the best welding condition. In addition, metallurgical assessments were performed to understand the effect of parameter combinations and pulse shape on bead-on-plate configuration.

Table 2 Operational parameters used in the pulsed Nd:YAG laser experiments

Characteristics	Values
Shielding gas	Argon, 15 l/min, 180 bar, 45°
Frequency	0.5 Hz
Overlap	0.5 mm
Welding speed	15 mm/min
Beam profile	Gaussian distribution

2 Experimental procedure

In this work, AA5083-H111 aluminium alloy with 3-mm thickness was pulsed laser welded under bead-on-plate configuration. The chemical composition is displayed in Table 1. For the experiments, an SYSMA pulsed laser equipment model M-D 100 W was applied with Nd:YAG source and the maximum 80 W average power and 9 kW peak power. Laser focus with Gaussian energy distribution was on the surface of aluminium with wavelength of 1064 nm. The welding setup is shown in Fig. 1, and the operational parameters selected are described in Table 2.

Statistical methods were applied to understand the influence of the main pulsed laser welding parameters on the joint quality, diminishing time, and cost consumption. In this matter, the design of experiment (DOE) approach and response surface metrology (RSM) were used with the Statgraphics software. After speculative welding trials, the preliminary results were used to define the range of parameters and generating the experimental DOE. Adopting the Box-Behnken Design (BBD) method, the experiments were conducted using rectangular pulse shape with three levels for each independent parameter: peak power, spot diameter, and pulse duration, as shown in Tables 3 and 4. The best arrangement of parameters was targeted to combine the lowest defect area with the higher penetration depth. Based on this assessment, the optimization achieved a new welding condition named "N." This welding condition was subjected to a further analysis changing from the original rectangular pulse shape to different configurations. In this sense, nine new trials were analysed varying peak power profile and pulse time, as illustrated in Fig. 2.

Weld seams appearances of all samples were macro and metallurgical analysed in transversal and longitudinal directions. The samples were metallographically prepared following the standard procedure of cutting, mounting, grinding, polishing, and subsequent Keller's reagent etching. Each condition was analysed in five different positions of the weld seam, except from the G condition (the central point of the BBD cube) that was performed in fifteen positions to assure the accuracy of the results. Qualitative and quantitative evaluations were performed. Total defect areas, including crack, porosity, and underfill, besides depth and width weld beads, were measured using ImageJ software, as shown in Fig. 3. These results were used to determine the weld aspect ratios, given by the quotient between depth and width diameter [28]. Besides, the power density was analysed by the quotient of the peak power to spot beam area

Table 3 Levels of the welding parameter applied in rectangular pulsed shape

Level	I	II	II
Peak power (W)	3150	3510	3870
Spot diameter (mm)	0.6	0.8	1.0
Pulse duration (ms)	5	12.5	20

Table 4 Combination of welding parameters according to BBD applied in rectangular pulsed shape

Condition	Peak power (W)		Spot diameter (mm)		Pulse duration (ms)	
	Level	Value	Level	Value	Level	Value
A	I	3150	I	0.6	II	12.5
B	I	3150	II	0.8	I	5
C	I	3150	II	0.8	III	20
D	I	3150	III	1.0	II	12.5
E	II	3510	I	0.6	I	5
F	II	3510	I	0.6	III	20
G*	II	3510	II	0.8	II	12.5
H	II	3510	III	1.0	I	5
I	II	3510	III	1.0	III	20
J	III	3870	I	0.6	II	12.5
K	III	3870	II	0.8	I	5
L	III	3870	II	0.8	III	20
M	III	3870	III	1.0	II	12.5

*Central point

[29]. The microstructure analysis was performed in the optimized samples using a Leica DM IRM optical microscope. Thermo Scientific Scios 2 scanning electron microscope (SEM) with an energy-dispersive X-ray spectrometer (EDS) was used to measure the chemical composition and evaluate the microstructure.

3 Results and discussion

3.1 Rectangular pulse shape

3.1.1 Weld bead analysis

The appearances of the top section from the weld seams performed using rectangular pulsed shape indicated the presence of some longitudinal cracks and spatter welding defects, as presented in Fig. 4. The optical analysis performed on the top view and cross sections showed that all welding combinations displayed some defects. Longitudinal cracks occurred along the centreline of the weld bead besides transversal cracks, voids, and underfill (Fig. 5).

The parameter variations from each welding condition delivered a specific energy density affecting the weld seams profiles. As shown in Fig. 6, the depth, the defect area, and the aspect ratio increase with the energy density. This fact is due to the weld seams made with a raising energy density displayed a higher heat concentration inside the melting pool, elevating the temperature and enhancing the weld depth. It was also observed a variation of mode welding in the aspect ratio slope curve, which changed from conduction

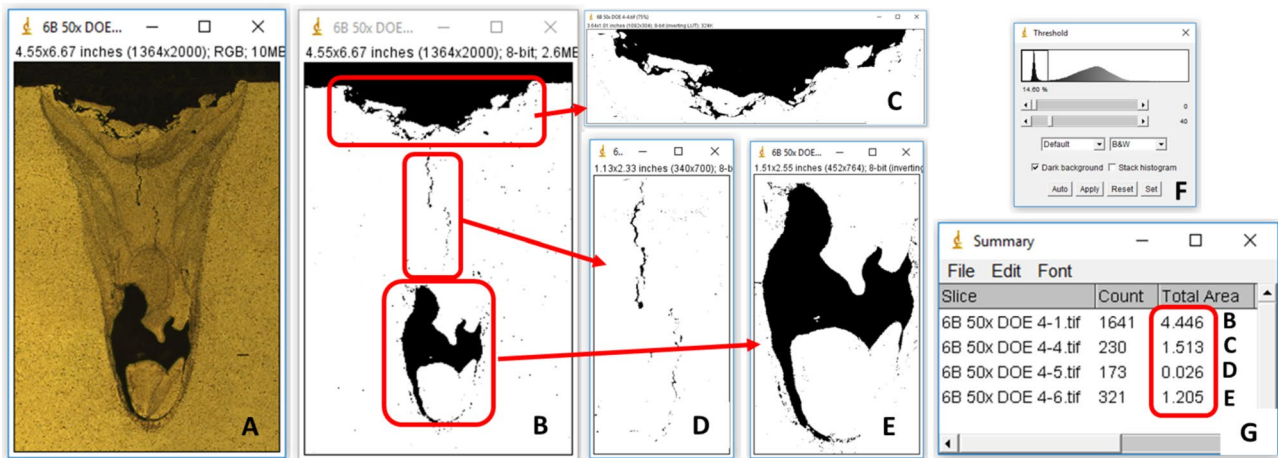**Fig. 2** Illustration of the different pulse profiles used in the optimized condition N
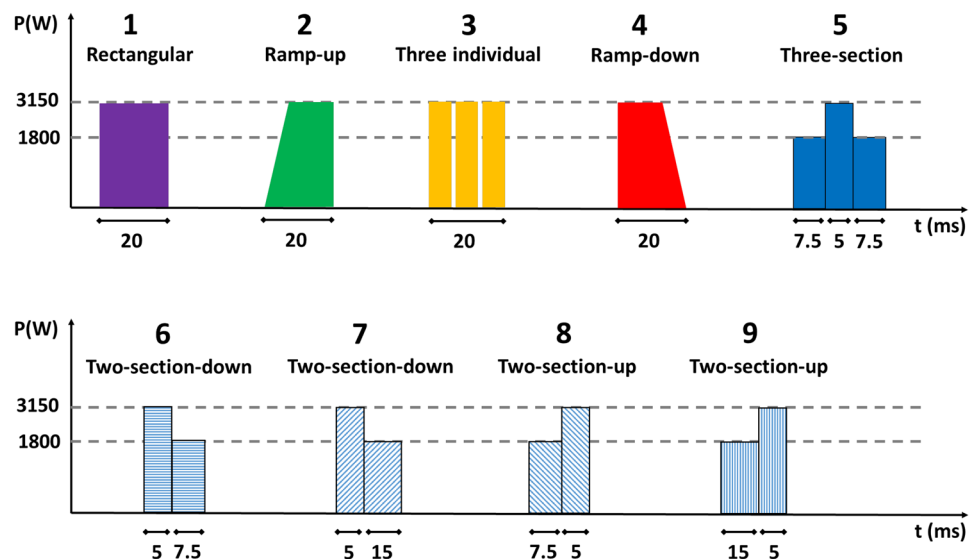
Fig. 3 Schematic diagram for defect analysing. Original macroscopic cross-section weld (**A**), binary image and defect selection (**B**), underfill (**C**), crack (**D**) and void (**E**), threshold panel (**F**), and, area measurements in pixels (**G**)

to keyhole mode. The lower values below 0.5 corresponded to conduction mode. Above 0.8, the welding regime displayed the intermediated mode, and higher values produced keyhole. A similar slope curve was presented by [30] in a study developed with a steel alloy. In terms of defects, welds made in conduct mode presented thin cracks and small pores, meanwhile in keyhole mode generated larger defects (voids and underfill). As noted, a maximum defect area occurred in the J condition with the aspect ratio of 1.88 and the deepest penetration.

3.1.2 Statistical assessment

From the standardized Pareto charts shown in Fig. 7, the spot size and peak power parameters considerably influenced the depth and defect aspects of the rectangular pulsed shape weld seams. However, the pulse time reflected a minor impact on the depth. Its effect was no statistically significant to produce defects with a level above the reference line, considered 5% of alfa. In the study performed in [11], SAE 1005 steel showed similar results with the depth strongly affected by the spot diameter.

BBD results displayed in both response surface charts (RSC) of depth and defect areas revealed similar behaviour (Fig. 8). The outcomes showed that the increase of peak power and reduction of spot diameter enabled producing deeper welds, besides facilitating the creation of the defect. In the same way, it reached the aspect ratio changing the pulse mode. The phenomena of keyhole developed in the laser process lead to defect presence due to the high levels of energy involved, which vapours the materials, creating voids and pores into the weld bead [28]. The best arrangement of parameters aimed at small defect areas with high depth resulted in the combination of 3195 W
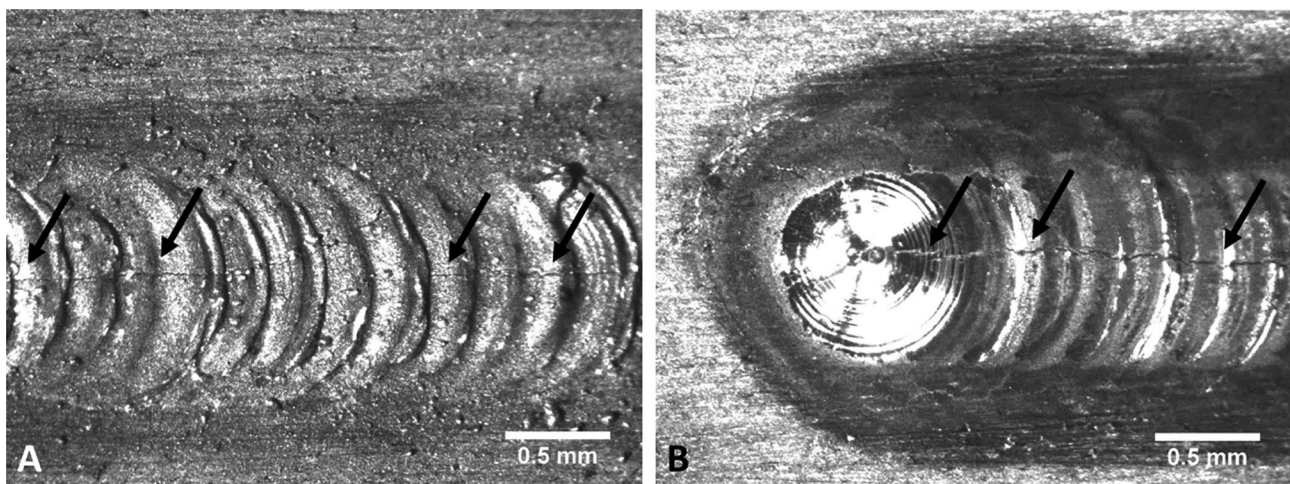

Fig. 4 Top view of AA5083 beads with spatters and longitudinal cracks
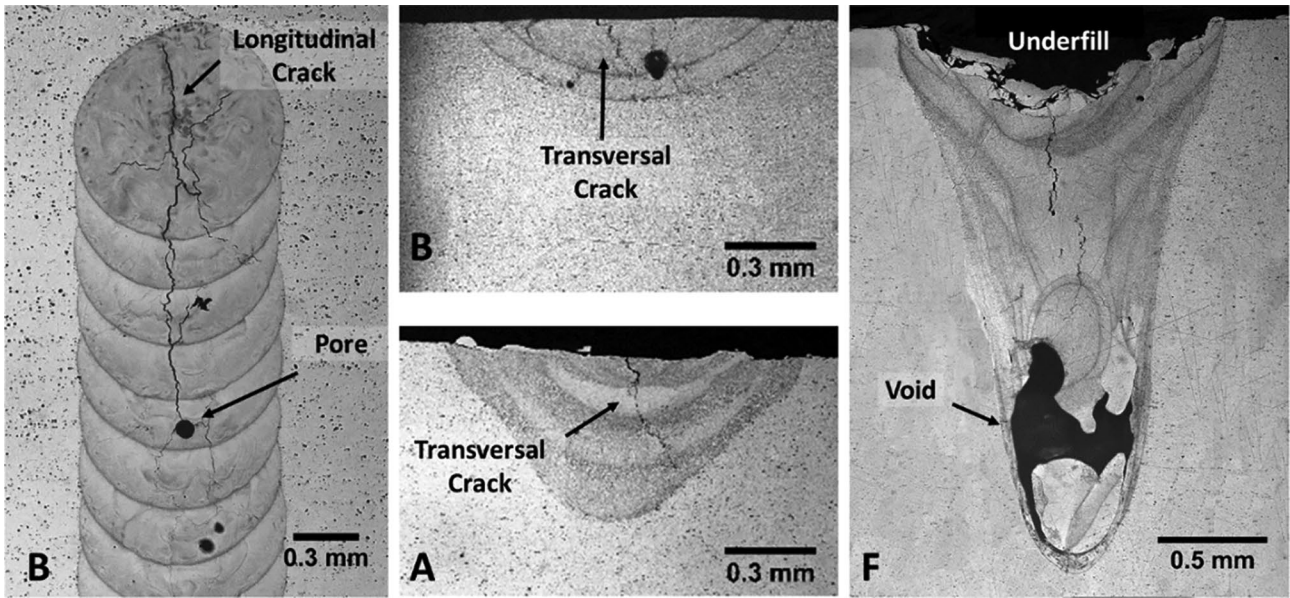
Fig. 5 Optical macrographs of the AA5083 weld beads (conditions from the Table 4) showing pores, underfill, longitudinal and transversal cracks

peak power, 0.7 mm spot diameter, and 20 ms pulse time with 8185 W/mm^2 energy density. As abovementioned, the pulsed time effect was no statistically significant to produce imperfections, and its increase improved the depth without substantially compromising the quality of welding.

3.2 Pulse shape variation

With the optimized response generated from rectangular pulse shape welds (N condition), a new set of weld seams was created, varying the pulse shape (as illustrated in Fig. 2). Conditions N1 to N4 had 0.7 mm of spot diameter, 20 ms

Fig. 6 Effect of peak power on the characteristics of the weld seams
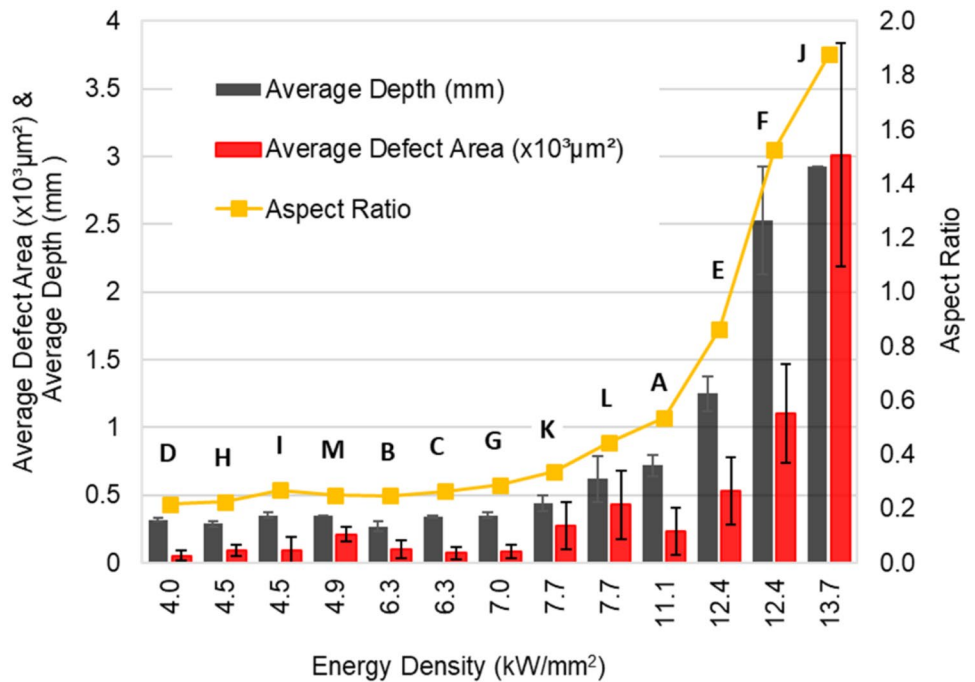
Fig. 7 Standardized Pareto charts of parameter effects in penetration depth and defect area
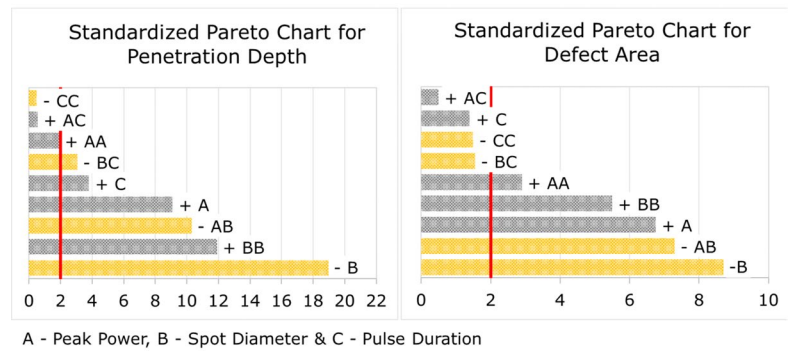
of pulse duration, and 3150 W of peak power, while N5 to N9 were made with different levels of peak power (1800 and 3150 W) and pulse duration. Therefore, the weld beads showed distinguished characteristics in terms of dimensions, defects, and microstructure, as demonstrated in Fig. 9 and Table 5.

Regarding the macrostructural aspects, all weld zones displayed similar shapes with aspect ratios between 0.26 and 0.28. The condition N4 created the largest melting area with the maximum depth of 0.32 ± 0.02 mm and width of 1.26 ± 0.02 mm. In contrast, condition N9 formed the smallest weld bead, with the lowest depth (0.27 ± 0.01 mm) and width (0.96 ± 0.03 mm).

Regarding the welding imperfections, several crack formations were noted along the centreline in most conditions, especially in N8 and N9. Both solidification cracking and liquation cracking were identified in the weld metal and HAZ. N3 displayed the highest area with $7.34 \pm 4.63 \times 10^{-4}$ mm^2 containing pores and transversal cracks. In contrast, the N5 condition generated the lowest level ($0.09 \pm 0.17 \times 10^{-4}$ mm^2) with small pores only. The effect of the pulse shape was evidenced through the difference between rectangular and three-section shapes,

where the defect area reduced about 98.4%. Crack-free weld zones were generated in conditions with the final step down stage, from N5 to N7 parameters. The prolongation of the cooling time from 7.5 to 15 ms (N6 and N7) reduced by a third the pore area. Similarly, a decrease of imperfections was noted with a higher heating time of 15 ms (N9) than 7.5 ms (N8).

Concerning the microstructural aspects, each beam profile generated a specific weld zone due to the different energy distribution and the heat flow created in the pulse shape. The modification in cooling rates induced by the local energy dissipation formed semi-circular band zones and the solidification front generated microstructure variations. As an intrinsic characteristic of this process, the intermittent energy input developed this pattern.

As expressed by Kou [31], the final microstructure is defined by the combined effect of the temperature gradient (G) and the growth rate (R). The mode of solidification is established by the ratio G/R, and the product GR will control the size of the solidification structure. In the studied samples, the welding region of a fusion zone (FZ) showed distinguished characteristics. The outer zone of the FZ, encoded as Zone III in Fig. 10, presented a planar dendritic zone, growth from
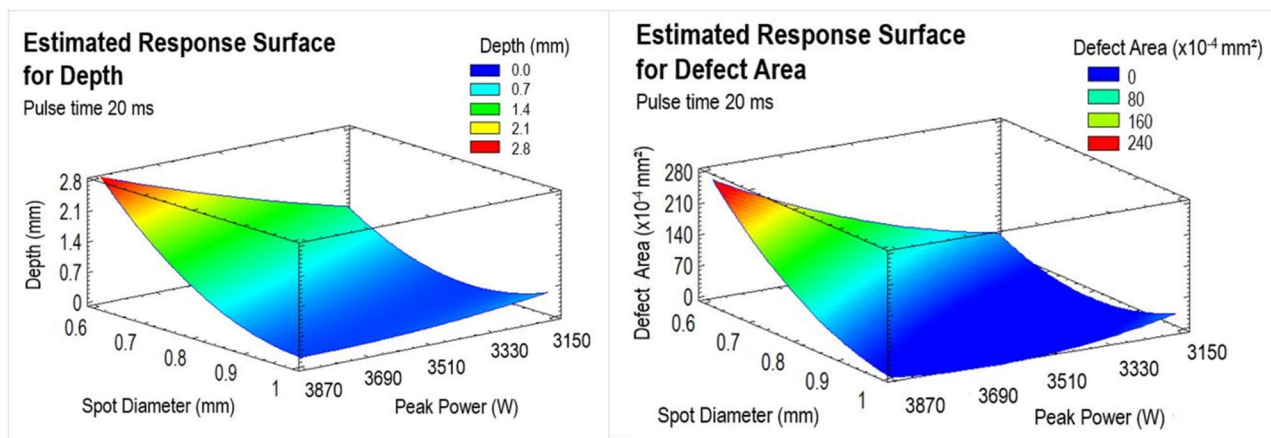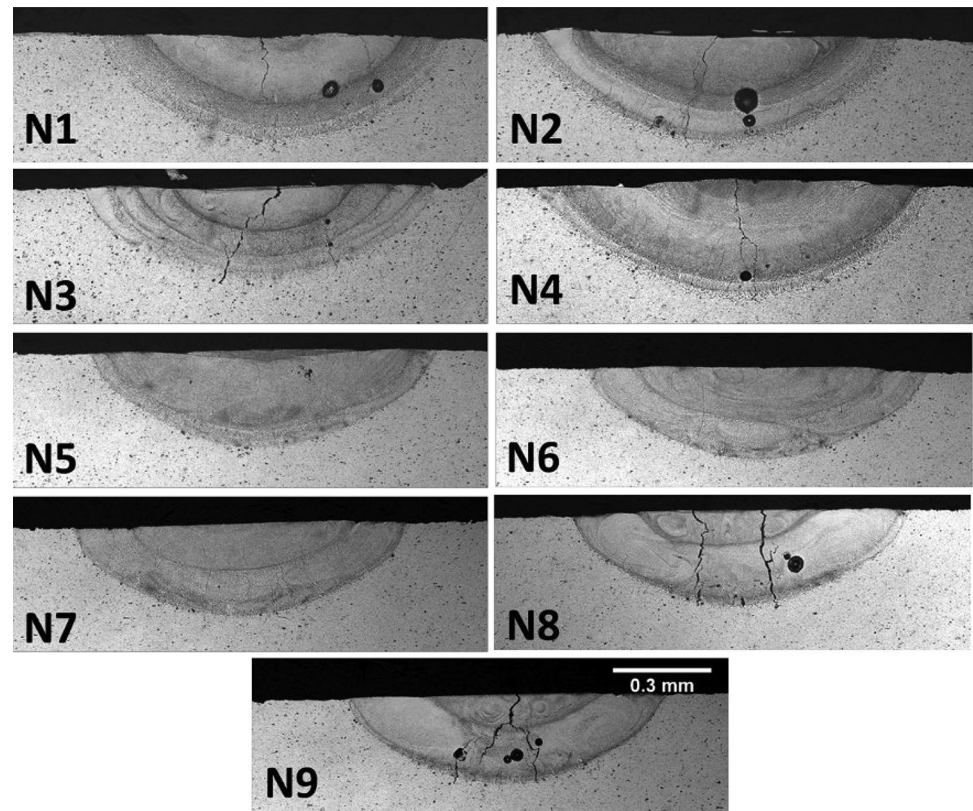

Fig. 8 Response surface plots estimated of 20 ms pulse duration for depth and defect area

Fig. 9 Cross section macrographies showing the optimized welding combination with different pulse shapes

the base metal, as a consequence of the solidification process with the highest temperature gradient. Beyond this band, a less severe solidification takes places, and the growth morphology changes to columnar dendritic structure, Zone II, also observed in previous researches [32–34]. Finally, a fine microstructure is developed in the upper and central region of the FZ, Zone I, in which a moderate temperature gradient controls the solidification. Therefore, the solidification mode changes from planar to columnar dendritic, and finally to equiaxial as the temperature gradient decreases [35]. In addition, by emitting intermittent pulses, the subsequent spot welds created another fusion boundary. This behaviour generated planar microstructure inside the previous weld pool, followed by columnar-dendritic (Fig. 11). This structure grew parallel to the local direction of maximum heat flow.

Figure 12 displays an example of the Fe–Al phases observed in the base material (BM). These precipitates were hardly noted in the centre of the fusion welding, and a reduced amount in the extremities of the weld zone near the dendritic microstructure was noted. This gradual enhancement indicates that the laser process probably dissolved them. This finding has been previously reported by authors in [5]. In this former study, SEM/EDS analyses revealed that Al–Mn–Fe–Si–Cr compounds are present in AA5083 base metal, but are dissolved at the fusion zone during the laser processing.

Table 5 Details of the weld beads produced with different pulse profiles (average values)

| Sample	Depth (mm)	Width (mm)	Aspect ratio	Defect area ($\times 10^{-4}$ mm^2)	Type of defect
N1	0.30 ± 0.01	1.17 ± 0.06	0.26	5.98 ± 4.58	Cracks, pores
N2	0.33 ± 0.01	1.21 ± 0.02	0.27	2.93 ± 0.69	Cracks, pores
N3	0.32 ± 0.02	1.19 ± 0.06	0.27	7.34 ± 4.63	Cracks, pores
N4	0.34 ± 0.01	1.26 ± 0.02	0.27	3.91 ± 0.85	Cracks, pores
N5	0.29 ± 0.01	1.04 ± 0.02	0.28	0.09 ± 0.17	Pores
N6	0.27 ± 0.00	1.03 ± 0.02	0.27	0.33 ± 0.47	Pores
N7	0.28 ± 0.01	1.06 ± 0.03	0.26	0.12 ± 0.24	Pores
N8	0.29 ± 0.01	1.01 ± 0.01	0.28	6.29 ± 1.03	Cracks, pores
N9	0.27 ± 0.01	0.96 ± 0.03	0.28	4.64 ± 2.00	Cracks, pores
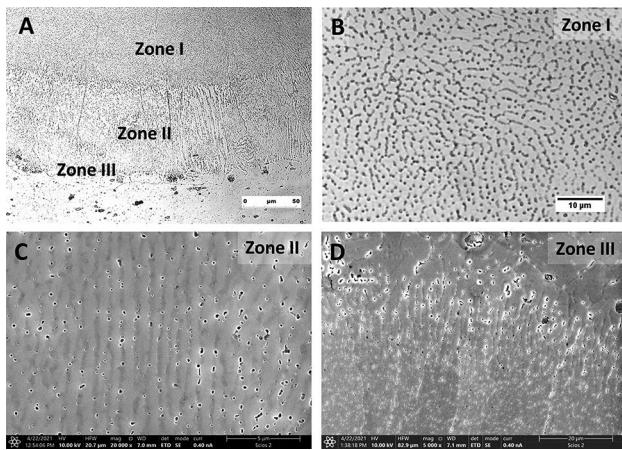
Fig. 10 Microstructure of the weld bead (**A**) showing the equiaxed grains (**B**) and columnar (**C**) grains of the FZ, and the interface of the weld zone (**D**)

The chemical composition of the BM and the FZ of the welded samples were measured by energy dispersive X-ray spectroscopy. Figure 13 displays the analysis of the BM and the N6 condition. All samples displayed Mg levels minor

than 4.2% that corresponded to the AA5083 base material, as shown in Fig. 14. The Mg evaporation from the weld pool was mainly a function of its low melting point (630 °C) and boiling point (1090 °C) [17, 24]. During the laser process, the material was subjected to high temperatures, enabling Mg evaporation and reducing the quantity detected.

Among the samples, the N6 condition developed a minor Mg reduction due to the lowest heat input involved. This profile did not have a heating step, and the peak power incidence lasted only 5 ms, followed by reduced cooling time (7.5 ms). This result is comparable to those obtained by Hekmatjou and Naffakh-Moosavy [2] in AA5456 alloy, where the amount of Mg decreased with the increase of preheating temperature.

The outcomes highlighted the effect of the pulse shape for controlling laser energy delivered. Changing the pulse shape promoted a significant influence in the heat input that directly affected the temperature gradient and the solidification rate of the liquid molten pool. When a final step with a decreasing energy profile was used, the laser beam continued irradiating the molten pool; this descending heat conserved the pool in the liquid state. As a consequence, the solidification rate was reduced enough to mitigate the cracking development. Even

Fig. 11 Microstructural evolution in the pulsed laser process showing the fusion boundary in the base material (**A**) and in the middle of the weld bead (**B**)
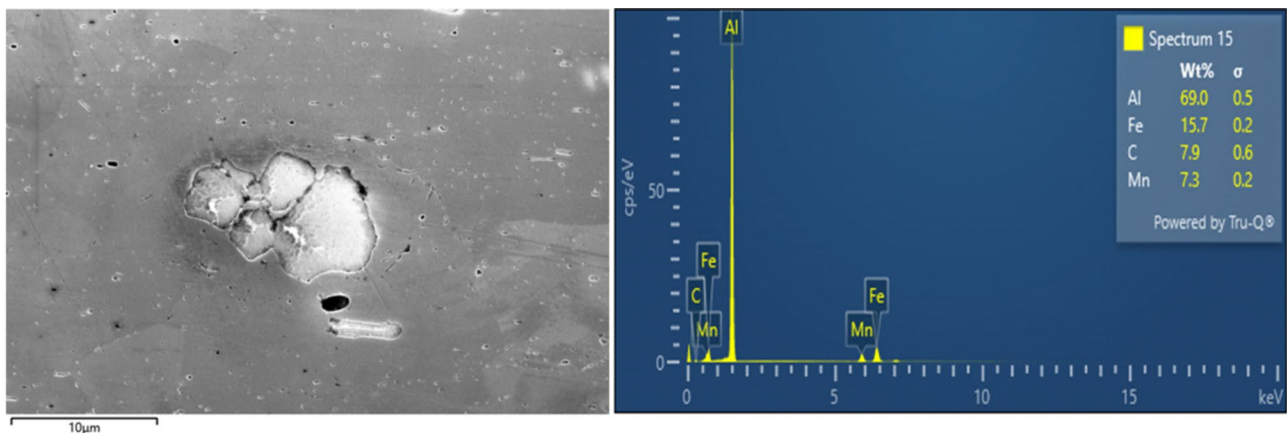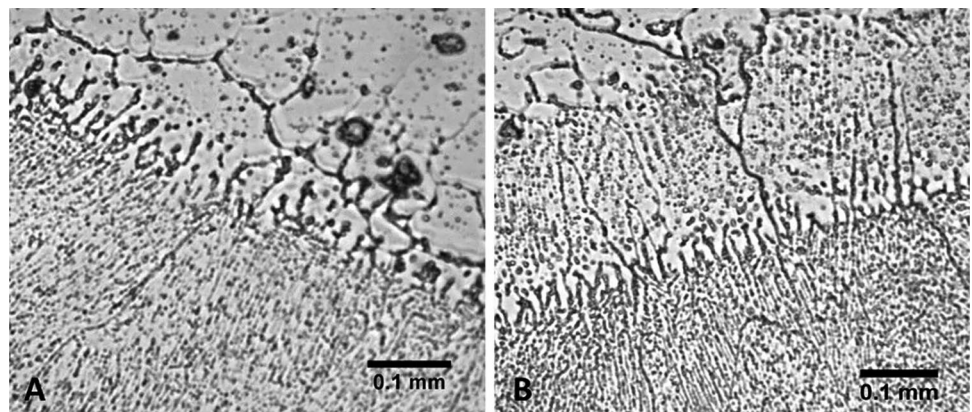

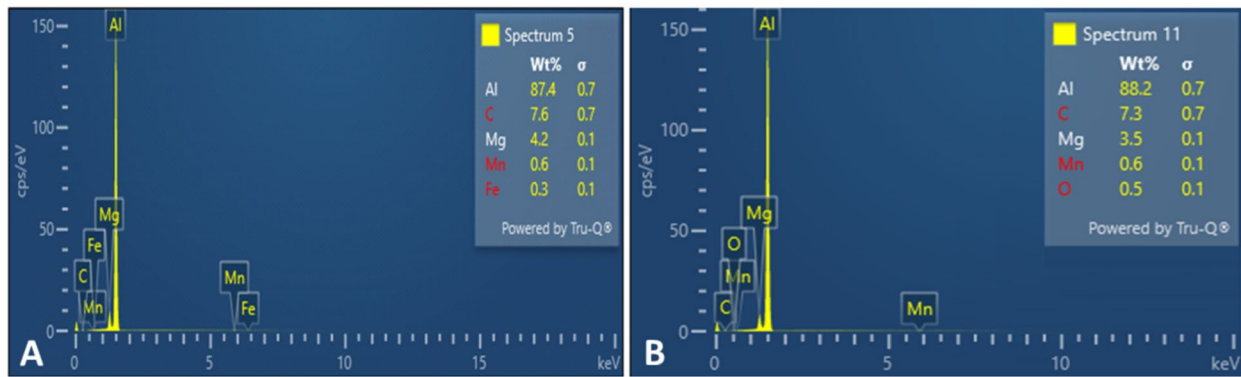**Fig. 12** Fe–Al phase observed in the BM and its EDS analysis

Fig. 13 EDS analysis of the BM (**A**) and FZ of the N6 condition (**B**)

being an extremely fast process, the gradient allowed the liquid metal to be supplied and backfilled and healed the cracks. This behaviour is a mechanism to reduce the shrinkage and thermal stresses in the weld metal.

Likewise, other studies of the pulse effect exposed similar positive results. Jia et al. [25] showed that the step-down and ramp-down profile applied on AA5083 achieved free crack weldments. In the same way, the same pattern of pulse shape impacted the pore densities in AZ31 magnesium alloy [24], where the slow cooling period condensed the pore area.

Besides the effect of the pulse shape, the intermittent pulse incidence also influenced the heat input. The overlapped area produced a high local temperature reaching the melting point and creating a new solidification interface inside the previously pulsed affected area. As a result, the heat dissipation varied once more, and the microstructure followed this cooling process. During this stage, the first structure to solidify was planar in the outer boundary layer. In the centre of the FZ, the columnar-dendritic or equiaxial crystals replaced this first structure due to the solidification process [31, 35].

Combining the results from microstructural analysis and the Mg variation effect, samples with a high amount of Mg hardly showed susceptibility to solidification cracking. Therefore, it was a result of the parameters applied in step-down mode. The slow cooling period developed a gradual decrease of power and mitigated the evaporation of

magnesium vapour in contrast with other peak profiles that generated higher evaporation and hot cracks. These results are in agreement with the increase of hot crack susceptibility observed at about 2% Mg in the AA5000 series [17, 20, 23].

4 Conclusions

AA5083-H111 welded with Nd:YAG pulsed laser was investigated using statistical and pulse shaping approaches. The peak power and spot diameter were the most influencing parameters to produce sound weldments. The optimization performed with the RSM indicated that the combination of 3195 W peak power, 0.7 mm spot diameter, and 20 ms pulse time achieved high depth and low occurrence of cracks and pores defects. After a trial of pulse shape variation using the optimized parameters, the pulse shape with the step-down stage reduced the crack formation and significantly diminished the pores density. These results showed a tendency to mitigate the defects by adding the post cooling stage, creating a behaviour associated with the gradual decrease of energy delivered to reduce the solidification rate in the molten pool. Therefore, the sensitivity to solidification cracking and the pores density can be mitigated or eliminated using the laser welding process with pulsed mode.
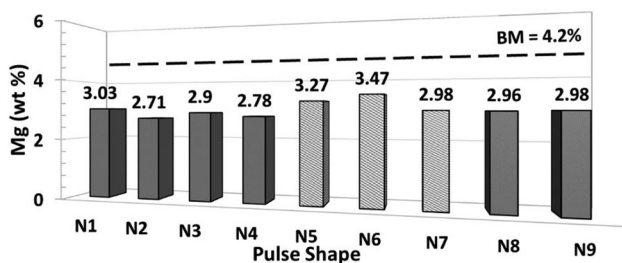
Fig. 14 Variation of the Mg element (wt%) at FZ of the different welds. The patterned bars correspond to the crack-free joints

Declarations

Ethics approval Not applicable.

Consent to participate Not applicable.

Consent for publication Not applicable.

Conflict of interest The authors declare no competing interests.

References

1. Abioye TE, Zuhailawati H, Aizad S, Anasyida AS (2019) Geometrical, microstructural and mechanical characterization of pulse laser welded thin sheet 5052–H32 aluminium alloy for aerospace applications. Trans Nonferrous Met Soc China 29:667–679. https://doi.org/10.1016/S1003-6326(19)64977-0
2. Hekmatjou H, Naffakh-Moosavy H (2018) Hot cracking in pulsed Nd : YAG laser welding of AA5456. Opt Laser Technol 103:22–32. https://doi.org/10.1016/j.optlastec.2018.01.020
3. Yang J, Li Y, Zhang H (2016) Microstructure and mechanical properties of pulsed laser welded Al/steel dissimilar joint. Trans Nonferrous Met Soc China 26:994–1002. https://doi.org/10.1016/S1003-6326(16)64196-1
4. Gordon MW (2003) Handbook of aluminum 1 New York
5. Sánchez-Amaya JM, Delgado T, De Damborenea JJ et al (2009) Laser welding of AA 5083 samples by high power diode laser. Sci Technol Weld Join 14:78–86. https://doi.org/10.1179/136217108X347629
6. Kuo TY, Lin HC (2006) Effects of pulse level of Nd-YAG laser on tensile properties and formability of laser weldments in automotive aluminum alloys. Mater Sci Eng A 416:281–289. https://doi.org/10.1016/j.msea.2005.10.041
7. Zhang G, Xiao C, Taheri M (2020) Effect of Nd:YAG pulsed laser welding process on the liquation and strain-age cracking in GTD-111 superalloy. J Manuf Process 52:66–78. https://doi.org/10.1016/j.jmapro.2020.01.049
8. Sheikhi M, Ghaini FM, Torkamany MJ, Sabbaghzadeh J (2009) Characterisation of solidification cracking in pulsed Nd:YAG laser welding of 2024 aluminium alloy. Sci Technol Weld Join 14:161–165. https://doi.org/10.1179/136217108X386554
9. Tzeng YF (2000) Parametric analysis of the pulsed Nd:YAG laser seam-welding process. J Mater Process Technol 102:40–47. https://doi.org/10.1016/S0924-0136(00)00447-7
10. Fang X, Zhang J (2015) Effects of microstructure and concavity on damage behavior of laser beam welded Ti-2Al-1.5Mn titanium alloy joints. Int J Adv Manuf Technol 79:1557–1568. https://doi.org/10.1007/s00170-015-6924-6
11. Chludzinski M, dos Santos RE, Churiaque C et al (2021) Pulsed laser butt welding of AISI 1005 steel thin plates. Opt Laser Technol 134
12. Hajavifard R, Motahari M, Özden H et al (2016) The effects of pulse shaping variation in laser spot-welding of aluminum. Procedia Manuf 5:232–247. https://doi.org/10.1016/j.promfg.2016.08.021
13. Chludzinski M, Eugenio R, Churiaque C et al (2021) Pulsed laser welding applied to metallic materials—a material approach. Metlas 11:1–34
14. Gao XL, Liu J, Zhang LJ, Zhang JX (2014) Effect of the overlapping factor on the microstructure and mechanical properties of pulsed Nd:YAG laser welded Ti6Al4V sheets. Mater Charact 93:136–149. https://doi.org/10.1016/j.matchar.2014.04.005
15. Malek Ghaini F, Hamedi MJ, Torkamany MJ, Sabbaghzadeh J (2007) Weld metal microstructural characteristics in pulsed Nd: YAG laser welding. Scr Mater 56:955–958. https://doi.org/10.1016/j.scriptamat.2007.02.019
16. Tzeng YF (2000) Process characterization of pulsed Nd:YAG laser seam welding. Int J Adv Manuf Technol 16:10–18. https://doi.org/10.1007/PL00013126
17. Beiranvand ZM, Ghaini FM, Moosavy HN et al (2019) Solidification cracking susceptibility in pulsed laser welding of Al–Mg alloys. Materialia 7:100417. https://doi.org/10.1016/j.mtla.2019.100417
18. O´Brien A, Guzman C (2007) Welding Handbook- Part 2 Welding Processes, Ninth Edit
19. Mathers G (2000) The welding of Al and its alloys. Woodhead Publishing Limited
20. Chua SF, Chen H, Bi G (2019) Influence of pulse energy density in micro laser weld of crack sensitive Al alloy sheets. J Manuf Process 38:1–8. https://doi.org/10.1016/j.jmapro.2018.12.035
21. Milewski JO, Lewis GK, Wittig JE (1993) Microstructural evaluation of low and high duty cycle Nd: YAG laser beam welds in 2024-T3 aluminum. Weld Journal-New York- 72:341--s
22. Jones IA (1996) Welding aluminium by laser. In: The International Conference on Advances in Welding Technology. Ohio USA p 899000
23. Rohde M, Markert C, Pfleging W (2010) Laser micro-welding of aluminum alloys: experimental studies and numerical modeling. Int J Adv Manuf Technol 50:207–215. https://doi.org/10.1007/s00170-009-2510-0
24. Zhang X, Cao Z (2019) Effects of pulse shaping on Nd:YAG laser spot welds in an AZ31 magnesium alloy. Opt Lasers Eng 119:1–8. https://doi.org/10.1016/j.optlaseng.2019.02.002
25. Jia Z, Zhang P, Yu Z et al (2021) Effect of pulse shaping on solidification process and crack in 5083 aluminum alloy by pulsed laser welding. Opt Laser Technol 134:1–9. https://doi.org/10.1016/j.optlastec.2020.106608
26. Mizutani M, Katayama S (1996) Mathematical modeling of fusion and solidification in laser welding and evaluation of hot cracking susceptibility. 25
27. Zhang J, Weckman DC, Zhou Y (2008) Effects of temporal pulse shaping on cracking susceptibility of 6061–T6 aluminum Nd:YAG laser welds. Weld J (Miami, Fla) 87:18–30
28. Katayama S (2013) Handbook of laser welding technologies. Woodhead Publishing Limited, Sawston, UK
29. Assuncao E, Williams S (2013) Comparison of continuous wave and pulsed wave laser welding effects. Opt Lasers Eng 51:674–680. https://doi.org/10.1016/j.optlaseng.2013.01.007

30. Buvanashekaran G, Siva Shanmugam N, Sankaranarayanasamy K, Sabarikanth R (2009) A study of laser welding modes with varying beam energy levels. Proc Inst Mech Eng Part C J Mech Eng Sci 223:1141–1156. https://doi.org/10.1243/09544062JMES1177

31. Kou S (2002) Welding Metallurgy. John Wiley & Sons Inc

32. Chowdhury SM, Chen DL, Bhole SD et al (2011) Microstructure and mechanical properties of fiber-laser-welded and diode-laser-welded AZ31 magnesium alloy. Metall Mater Trans A Phys Metall Mater Sci 42:1974–1989. https://doi.org/10.1007/s11661-010-0574-y

33. Xiao L, Liu L, Zhou Y, Esmaeili S (2010) Resistance-spot-welded AZ31 magnesium alloys: Part I. Dependence of fusion zone microstructures on second-phase particles. Metall Mater Trans A Phys Metall Mater Sci 41:1511–1522. https://doi.org/10.1007/s11661-010-0197-3

34. Zhou J, Tsai HL, Wang PC (2011) Hybrid laser-arc welding of aerospace and other materials. Woodhead Publishing Limited

35. Lippold JC (2015) Welding metallurgy and weldability. John Wiley & Sons Inc

Publisher's Note Springer Nature remains neutral with regard to jurisdictional claims in published maps and institutional affiliations.